Earthquake rupture tracking with six degree-of-freedom ground motion observations: a synthetic proof of concept

Kilian Gessele [1], Shihao Yuan [1], Alice-Agnes Gabriel [1], Dave A. May [2], Heiner Igel [1]

[1]Department of Earth and Environment Sciences, Ludwig-Maximilians-Universität München, Munich, Germany.
[2]Department of Earth Sciences, University of Oxford, Oxford, United Kingdom.

Key Points:

- We demonstrate concepts for earthquake rupture imaging from combined translational and rotational motions.
- We show that S-waves can be used for earthquake rupture tracking due to the wavefield separation in rotational components.
- We discuss effects of directivity, supershear rupture speeds and source-receiver geometry.

Corresponding author: Shihao Yuan, syuan@geophysik.uni-muenchen.de

Abstract

With the availability of new instrumentation for more complete ground motion measurements, as rotation or strain measurements using optical technology, novel application opportunities in seismology arise. Back azimuth information can be determined from combined measurements of rotations and translations at a single site. Such six degree-of-freedom (6-DoF) measurements are reasonably stable in delivering similar information compared to a small-scale array of three-component seismometers. Here we investigate whether a 6-DoF approach is applicable for imaging earthquake rupture propagation. While common approaches determining the timing and location of energy sources generating seismic waves rely on the information of P-waves, here we take S-waves into account. We analyze 2-D and 3-D synthetic cases of unilateral but complex rupture propagation. The back azimuths of directly arriving SH-waves in the 2-D case, and P-converted SV-waves and SH-waves in the 3-D case are tracked. For data analysis in terms of wave polarity we compare a cross-correlation approach using a grid-search optimization algorithm with a polarization analysis method using point measurements. We successfully recover rupture path and rupture velocity with only one station, under the assumption of an approximately known fault location. Using more than one station, rupture imaging in space and time is possible without a priori assumptions. We demonstrate robustness of the approach in resolving relatively small variations of rupture velocity, and rupture jumping across off set fault segments. We discuss the effects of rupture directivity, supershear rupture velocity, source-receiver geometry as well as potential and challenges for the method.

1 Introduction

The path and speed of large earthquakes are crucial factors determining their damage potential. Rupture kinematics can be routinely determined by finite-fault inversion approaches based on close fitting of observations through the use of a large number of free parameters. However, despite recent advances (e.g., Shimizu et al., 2019), kinematic models typically need to pre-define fault geometry, are characterized by inherent non-uniqueness (Mai et al., 2016) and do not ensure mechanical consistency in terms of earthquake dynamics (e.g., Ulrich et al., 2019).

The rise of large-scale, dense seismic array instrumentation has enabled complementary techniques tracking earthquakes in space and time (e.g., Kiser & Ishii, 2017). Such methods image coherent high-frequent energy radiation (not slip) in simple and rapid manners requiring very limited a priori knowledge.

Here, we present proofs of concept for earthquake rupture imaging with single-site point measurements combining rotational and translational components of the seismic wave field. We study the polarity of directly incoming SH- (in 2-D and 3-D) and P-converted SV-waves (in 3-D) of synthetic 6-DoF time series.

First, we introduce two distinct single-station approaches for estimating the direction of incoming waves, namely a cross-correlation approach using a grid-search optimization algorithm and a polarization analysis method using point measurements. Then, a statistical approach for combining the back azimuth estimates of several stations is presented which shows a high resistance concerning measurement uncertainties. We verify the concept in synthetic 2-D experiments analysing SH-wave polarity and discuss the applicability and robustness of the developed methodologies. Finally, we demonstrate earthquake rupture tracking in 3-D media from the rotation polarization caused by P-converted SV-waves and direct SH-waves. We analyze the effect of interfering arrivals and non-uniform slip rate distribution. We discuss source-receiver scales and geometry as well as challenges of the method for future global applications.

1.1 Earthquake rupture tracking

Most common techniques to image earthquake properties using array data can be divided into two categories which are both based on analyzing the phase information of P-waves. In contrast to finite slip inversions, no detailed knowledge of Green's functions and source properties is necessary. Methods of the first category are based on conventional array measurements. Termed back-projection methods, seismic energy radiation is imaged by applying array beam-forming techniques. Back-projection was for the first time successfully demonstrated for the 2004 Sumatra-Andaman Earthquake (Krüger & Ohrnberger, 2005; Ishii et al., 2005). Directivity effects were utilized to characterize faulting mechanisms (Ammon et al., 2005).

Methods of the second category track earthquake rupture by estimating the back azimuth (BAz) of incoming waves with a single-station. In polarization analysis, the three translational components of standard seismometers can be used to estimate the BAz and incidence angle of incoming waves (Flinn, 1965; Montalbetti & Kanasewich, 1970; Vidale, 1986; Greenhalgh et al., 2005). Bayer et al. (2012) developed a single-station approach to track moving sources by polarization analysis of local and regional P-wave arrivals. They normalize the BAz variation with respect to the known hypocenter. Frohlich & Pulliam (1999) pointed out that, compared to traveltime-based methods, classic single-station approaches suffer from several ambiguities, as for example 180° BAz errors. The joint analysis of translational and rotational motions can help overcome such drawbacks.

1.2 6-DoF ground motions

The complete wavefield excited by an infinitesimally small deformation can be described by the three components of translation, three components of rotation, and six components of strain (Aki & Richards, 2002). However, until recently, seismology is dominated by translational observations (vertical, N-S, E-W), sometimes combined with strain measurements. Translational motion is the movement of a particle along an axis. In contrast, rotational motion describes the particle movement around an axis. Information on rotations has been widely ignored, mainly, because of measurement difficulties. 6-DoF information is obtained from measuring in addition to three translational components also three components of rotational motion. This increase of information compared to classical observations has the potential to improve existing methods and creates new opportunities for research and industry (e.g., Igel et al., 2015; Schmelzbach et al., 2018). Until recently rotational motions have been derived from arrays of conventional single or multi-component sensors (e.g., Spudich et al., 1995; Huang, 2003; Suryanto et al., 2006; Spudich & Fletcher, 2009). However, these methods are limited by array spacing as well as local heterogeneities and site effects. Classic translational measurements are also sensitive to tilt, i.e., the horizontal components of the rotation vector (van Driel et al., 2015; Graizer & Kalkan, 2008).

Recent advances in fibre-optic gyroscopes and ring laser-based sensors show that applicable, single-station measurements for translation and rotation are within reach (Schreiber & Wells, 2013; Bernauer et al., 2012, 2018). The earthquake source process and the interaction of the wavefield with a free surface or heterogeneities of the Earth can excite rotational ground motions. In isotropic media the rotational motion $\boldsymbol{\omega} = (\omega_x, \omega_y, \omega_z)^T$ can be described by a linear combination of spatial derivatives of the translational particle displacement motion $\boldsymbol{u} = (u_x, u_y, u_z)^T$ (e.g., Cochard et al., 2006):

$$\begin{pmatrix} \omega_x \\ \omega_y \\ \omega_z \end{pmatrix} = \frac{1}{2}\nabla \times \boldsymbol{u} = \frac{1}{2} \begin{pmatrix} \partial_y u_z - \partial_z u_y \\ \partial_z u_x - \partial_x u_z \\ \partial_x u_y - \partial_y u_x \end{pmatrix}, \tag{1}$$

where $\times$ denotes cross product and ∂_k denotes spatial derivatives with respect to x_k. The same relation is valid for the time derivatives, the rotation rate $\dot{\boldsymbol{\omega}}$ and particle velocity $\boldsymbol{v}$. At the free surface, the stress-free boundary condition is slightly modified (e.g., Schmelzbach et al., 2018). While inside isotropic media the curl operator separates the S-wave field, in anisotropic media even (quasi-)P-waves can have a rotational component (Pham et al., 2010). Local phase velocities and the BAz can be estimated from 6-DoF measurements at a single-station due to the relation between translations and rotations (Pancha et al., 2000; Igel et al., 2007; Hadziioannou et al., 2012; Edme & Yuan, 2016; Sollberger et al., 2018).

2 Methodology

2.1 BAz estimation - single station approach

We first test two different methods to track earthquake rupture in simple 2D examples. Both methods are based on a plane wave assumption and analyze the polarity of directly arriving SH-waves at a single station. Since the region of energy radiation moves during the rupture across the fault plane, we utilize sliding windows moving throughout the signal to determine the evolution of the signal source direction. In each time window, the BAz is estimated and a temporal trend can be derived by comparing all windows. When this information is combined with a priori knowledge on the fault or with data from other stations, the rupture propagation and its velocity can be estimated.

The CC (cross-correlation) method is a grid-search optimization algorithm that relies on the interdependence of transverse translational motion and vertical rotation. The CC is a measure for the similarity between two signals and the CC coefficient provides a measure for the degree of similarity (see Fig. 1). A CC coefficient of 1 implies perfect similarity, a value of -1 means anti-correlation.

Similar to the approach by Igel et al. (2007), we estimate the BAz by rotating the horizontal acceleration components in small steps around all possible BAz ($0° - 360°$) and cross-correlating successively with the vertical rotation rate. A zero-lag normalized CC coefficient is used. For a noise-free signal, the CC coefficient in the grid-search is a function without a clear maximum. It is a step-function that jumps from -1 to 1. Therefore, we use the two zero transitions of the step-function instead of the global maximum. We expect that the central position between the zero transitions corresponds to the actual BAz.

The second method was introduced by Sollberger et al. (2018) and we refer to it hereinafter as polarization analysis. In comparison to the CC method it is more flexible and can be applied to P-, SV-, SH-, Rayleigh- and Love-waves. Instead of a MUSIC likelihood function (Schmidt, 1986), we use one based on classical power spectrum, because we expect a more stable result. We assume that the global maximum of the likelihood function is related to the actual BAz. It is necessary to define a parameter space for evaluating the likelihood function in a grid search. While the CC method requires the definition of the BAz increments, the increments for the S-wave velocity and the incident angle must be additionally defined for the polarization analysis. Both methods are illustrated for a plane wave in Fig. 1.

[Figure 1 about here.]

The difficulty of retrieving BAz (source directivity) from 3-D observations with solely translational motions is due to two challenges:

1) the 180° ambiguity in BAz estimates if only translational motions are recorded (Langston & Liang, 2008). Considering that rotational motions are essentially the curl of translational motions, the polarity of rotation will reverse in case of an opposite propagating direction while translation polarity remains unchanged. Thus joint analysis of rotation and translation will help to remove the 180° ambiguity when locating the sources.

2) translation records suffer from interfering different types of wavefields at the free surface, i.e., P- and SV/SH-waves, Rayleigh- and Love-waves are generally intermixed in recorded horizontal components. However, rotational motions naturally separate P- and S-waves as P-waves do not generate rotational motions in isotropic media. SV- and SH-waves (the same as Rayleigh- and Love-waves) are also naturally separated despite unknown source locations since SV-waves or Rayleigh-waves only generate rotational motions on horizontal components while SH related (Love-wave related) rotational motions being isolated on vertical components. We can therefore take advantage of the fact that two horizontal rotational components contain exclusively SV- or Rayleigh-waves.

Without the interference of other types of waves, the ratio between the two horizontal rotational components is directly related to the BAz according to:

$$\theta_{BAz} = \arctan\left(\frac{\omega_n}{\omega_e}\right), \tag{2}$$

where ω_n and ω_e denote the north-south and east-west components of rotation (or rotational rate in this study). This simple relationship is specially useful for estimating source directivity and it is independent of any possible radiation pattern that the source might have (Langston & Liang, 2008).

2.2 Combining many stations - probabilistic synthetic approach

It is possible to track the horizontal propagation of a rupture with only one station, presupposed the BAz changes correctly determined in a seismogram and the fault position is known a priori. An infinitesimal thin ray could be constructed for each estimated BAz in the direction of the directly arriving waves. The intersections of these rays with the fault position would show the temporal evolution of the rupture. In case of an unknown fault, at least two stations are necessary for the tracking process. But for more than two stations the rays will not intersect in exactly one point, since measurement errors and inaccuracies in the methodology can not be excluded completely. We want to take these uncertainties in the BAz into account by using wider beams instead of infinitesimal thin rays. We define the shape of each beam by a normal distributed probability density function $p(x, y, t)$ given by

$$p(x,y,t) = \sum_{i=1}^{N_{\text{stations}}} \frac{1}{\sqrt{2\pi\sigma_i(t)^2}} \exp\left(-\frac{1}{2}\left(\frac{\Phi_i(x,y,t)}{\sigma_i(t)}\right)^2\right), \tag{3}$$

where the standard deviation $\sigma_i(t)$ is defined individually for each station i, $\Phi_i(x,y,t) \in [0, 180°]$ denotes the angular distance from an arbitrary point in space to the estimated BAz of a specific station i and N_{stations} denotes the number of stations. Note that the probability density function is a time dependent function and is defined for each horizontal position (x, y). The time framework is defined in such a way that $t = 0$ corresponds to the first arrival at a station. For a specific time-step t_0 the amplitudes of all beams are added up and we assume that the most likely source position is close to the maximum value of $p(x, y, t_0)$. In Fig. 2 we show examples of probability density functions for different BAz errors and a 2-D representation of $p(x, y, t_0)$ for two stations using Eq. 3 with $N_{\text{stations}} = 2$.

[Figure 2 about here.]

3 Synthetic case studies in 2-D

In the following, we use data of elastic wave simulations in 2-D to demonstrate possible applications on a fundamental level and their limitations. We describe two different test cases. The fault position is known in the first case and we try to track the spatial and temporal evolution with only a single station. In the second case, we assume that the fault position is unknown and the individual results of many stations are combined.

3.1 Rupture tracking with a single 6-DoF station

We model a pure strike-slip earthquake embedded in a 2-D homogeneous medium. The unilateral rupture has a constant speed of 80% of the shear velocity v_s and it is implemented in as a line of double-couple point sources. We choose the source time function of each point source to be an ordinary Gaussian. Additionally, we slightly randomize the onset time and the seismic moment to render our synthetic study more realistic. 2-D wave propagation simulations are performed using the spectral element package `se2wave`. The mesh representation and support for MPI parallelism in `se2wave` is provided via PETSc (Balay et al., 2019, 1997).

Fig. 3 visualizes the model setup and tracking results of a unilateral rupture that propagates from north to south. We illustrate the receiver and fault setup in the upper panel, in which the stations are represented by two blue triangles. The a priori known fault position is marked by a grey dashed line and the unknown rupture trace by a red line.

Each station records the horizontal accelerations a_x, a_y and the vertical rotation rate $\dot{\omega}_z$ of the directly incoming P- and S-waves (middle panels of Fig. 3). These seismograms demonstrate that P-waves do not have a rotational component in an isotropic and homogeneous medium. Station A only records weak P-wave amplitudes due to the perpendicular position with respect to the rupture. Due to different BAz between source and station, the duration of the SH-arrivals is different for station A and B. The maximum expected BAz variation for station A is about 11.5° and 5° for station B. We estimate the BAz changes by moving a sliding window of 1.5 s length through the SH-wave signal of the seismograms.

In each window the BAz is estimated by the polarization analysis and the CC method and the results are illustrated in the bottom subplots of Fig. 3. Each point in these graphs represents the central position of a time window. The points are color-coded relative to the first and last SH-wave arrival. Both methods provide the same linear trend and the results are nearly perfectly overlapping.

We include a graphical representation of the resulting BAz estimates in the upper panel of the same figure in the form of color coded thin rays for each estimated BAz, respectively. The rays show a clear trend for both stations from north to south. The horizontal dimensions of the rupture are tracked correctly.

If the rupture or a certain part of the rupture has a constant rupture speed and the starting and ending point are approximately known, it is possible to estimate the rupture speed by trigonometric considerations. The rupture speed depends on the S-wave velocity, the rupture length, the rupture duration measured at the receiver and the orientation of rupture direction and receiver. Both bottom plots in Fig. 3 are divided in three subwindows. We determine the velocity in each sub-window by fitting a straight line through the estimated BAzs and express it relative to the known S-wave velocity. In all subwindows a rupture velocity is estimated that is close to the real value of 80% v_s.

[Figure 3 about here.]

3.2 Direct estimates of rupture velocity

We evaluate the sensitivity of the proposed 6-DoF tracking methods to variations in earthquake rupture propagation speed across the fault. Reliable, far-field estimate of rupture velocity is important to constrain earthquake dynamics, stress drop, and implications for seismic hazard but is inherently difficult because of the intermixing of rupture geometry and rise time in controlling the P- and S-wave pulse shapes (e.g., McGuire & Kaneko, 2018). We test three different rupture scenarios. The model setup is the same as in the previous 2-D tests, but here only the first half of the rupture has a constant speed of 80% v_s. The second half breaks with a constant velocity of 40%, 60% or 150% of v_s. Earthquake ruptures can propagate at sub-Rayleigh or at intersonic speeds (e.g., Archuleta, 1984; Gabriel et al., 2012) and a speed of 150% v_s means that the rupture is propagating faster than the radiated SH-waves. This effect is referred to as super-shear rupture speeds.

In Fig. 4 we estimate the BAz changes for each case of velocity variation at station A in the same way as in Fig. 3. Each column represents the result for a specific velocity jump. The BAz results are divided into three subwindows, in which the rupture velocity is calculated, respectively. The final velocity results, which we express relative to the shear-wave velocity, are illustrated for each subwindow by a red horizontal line in the lower panels. We indicate the true rupture speed by blue dashed lines. In each test scenario there is a significant increase or decrease visible from the starting velocity of 80% v_s in the first subwindow to the final rupture velocity of 40%, 60% and 150% in the last subwindows. While the speed of the second half of the rupture is determined nearly perfectly, the starting velocity is slightly underestimated.

[Figure 4 about here.]

3.3 Rupture tracking in heterogeneous media

We expect that 6-DoF rupture tracking is more difficult in heterogeneous materials, since reflected and scattered energy will contaminate the directly arriving SH-waves. We rerun the simulation of Fig. 3 now perturbing the homogeneous model by adding a normally distributed random material heterogeneity. We add variation of up to $\pm 5\%$ to density, P-wave and S-wave velocity in the medium. In the numerical simulations quadrilateral elements are employed, each possessing piece-wise constant material properties and edge lengths ~ 100 m. Material properties in each element are perturbed independently of each other and no smoothing of the piece-wise constant properties is applied between neighbouring elements.

The seismograms recorded at station A are shown in Fig. 5. Because of reflections in the material, P- and S-waves are no longer perfectly separated. Reflected phases are visible in all components after the dominant SH-arrival. The lower panel shows the tracking result, in which the true starting and ending BAzs for station A are marked by blue dashed lines. The spatial dimensions of the rupture are nearly perfectly estimated. Although we expect a nearly straight line for the temporal evolution, there are higher deflections than in the homogeneous model. However, on average a rupture speed of 77% v_s is determined, which is very close to the true velocity. The BAz deflections are increasing for stations in the higher distance and for stations that are placed in a geometrical orientation, in which the SH-wave amplitudes are less dominant compared to the P-wave amplitudes.

[Figure 5 about here.]

3.4 Rupture tracking for unknown simple and complex rupture paths and directivity effects

Rupture tracking with only a single station is possible if the fault or more explicitly the rupture path is known a priori. In the following, we assume that the fault position is unknown. Since a single station is not enough to track the rupture in this case, we here combine the BAz estimates of many stations. The BAz is still calculated in a single-station approach at each receiver, but the final tracking results of all stations are combined.

As described in section 2.2, for a certain time-step we send an imaginary beam back from each station in the direction of the rupture. By using a broad beam instead of a thin ray, we here take BAz uncertainties into account. We add up the amplitudes of all beams and the maximum is expected to be the most likely source point. The station coordinates and the BAz changes at each receiver are the input parameters for Eq. 3.

However, there is another issue that is referred to as a consistent time-frame. Due to different BAz between stations and rupture, the SH-arrivals at each station have a varying length of time (compare to the seismograms of Fig. 3). The time-shift of the sliding window has to be corrected at each station for this effect. Otherwise, an offset of the estimated rupture position from the actual location is expected, even if the BAzs are correctly determined. Previous studies neglect such directivity effects expecting only small deviations.

First, we verify that a 6-DoF method provides accurate results for simple and more complex fault geometry then we discuss the importance of directivity effects. We apply a time correction to the BAz estimates by assuming that the start and the end of the directly arriving SH-waves is visible in the signal. This is done in the rotational component of ground motions due to its high sensitivity to shear motions.

In the following, we track a simple unilateral rupture at five stations. The stations are placed in an asymmetrical pattern around the rupture with different distances to the source. The stations are situated in such a way that the resolution is about the same for both spatial dimensions. The medium and rupture parameters are equal to the homogeneous model in the previous section. The SH-waves at each station are picked manually and the BAz change is independently determined of the other stations. In Fig. 6 rupture tracking results are shown for three different time-steps (a, b and c). The estimated starting position is shown in Fig. 6a and the ending position in Fig. 6c. Animation S1 visualises the continuous rupture imaging (Movie S1: ms01.mov).

In the first subplot of Fig. 6, we show the arrangement of rupture (red line) and stations (white triangles). The following subplots are zoomed in the source location and the red dots show the estimated source points. The background color-map represents Eq. 3 as a two dimensional function. It is more likely that the current rupture position is in the vicinity of a point with bright colors than of a point with dark colors. The results of all stations are equally weighted. For each time-step, the current estimated source location is represented by a black star and previous most likely positions are marked by white crosses. The beams of all stations intersect nearly perfectly in one position. An unambiguous trend from top to bottom is visible and the white crosses match the red rupture line.

[Figure 6 about here.]

We repeat the same experiment as presented in Fig. 7 for a more complex rupture geometry. An animation of the continuous rupture imaging for the complex rupture geometry is provided in the supporting material (Movie S2: ms02.mov). The rupture propagates on three horizontally displaced segments of different lengths. The four subfigures show the rupture tracking at different time steps. Even in this more complex situation the rupture is correctly tracked and the fault offsets are visible in the final tracking results.

[Figure 7 about here.]

The length of time during which body waves arrive directly varies for different station locations in dependence on the rupture position. Such directivity effects will cause artifacts in the tracking result if the information of many stations is combined. In both previous experiments, we correct for directivity effects by picking the start and end time of the SH-arrivals in the seismograms. We expect that, in real data, it is difficult to determine the last arrival of the SH-waves, although the rotational observation facilitates the identification of shear waves.

Thus, an important question arises: How is rupture tracking affected if only the first arrival is visible in the seismograms? Bayer et al. (2012) neglected directivity effects in a comparable approach with classic 3C data for P-waves and used the same time-shift for the BAz estimation window. While conventional back-projection does not include a time correction for directivity effects (e.g., Ishii et al., 2005) , P-wave based rupture tracking utilizing beam-forming has been shown to require correction for the varying locations of the seismic sources (e.g., Krüger & Ohrnberger, 2005).

Fig. 8 illustrates the impact of directivity effects in an additional numerical experiment. The rupture is tracked by a small array of four stations which has a relatively small opening angle. The influence of directivity effects is expected to be significantly smaller for an array with small opening angle. However, if the angle is too small, it is not possible to determine both spatial dimensions of the rupture in good quality. In Fig. 8 the station positions are shown in the first map. In the left subplot, we show the final result for estimation in which we corrected for directivity effects. The resolution of the x coordinate is not as excellent as in the previous results, since a smaller array is used, but the rupture is still tracked correctly. The right subplot shows the result for the same data, but this time the time-shift of the sliding window in the BAz estimation is assumed the same for all stations. The starting position is still correctly determined but later estimated points show a systematic deviation from the true rupture path. Even if the rupture area and its linear trend are roughly tracked, the geometry is not correctly derived. By neglecting directivity effects it is possible to track the beginning of the rupture, but not its complete spatial evolution.

[Figure 8 about here.]

4 Rupture tracking in 3-D heterogeneous media

We extend the presented 2-D findings by examining the stability and accuracy of 6-DoF rupture tracking in 3-D heterogeneous media where multi-phases interfere with each other.

The opening angle for a certain earthquake, i.e., the detected BAz variation, depends on epicentral distance and station azimuth. The resolving power at a single station will potentially decrease with the increasing epicentral distance while increase with the increasing inclination angles. In the following, we first estimate the expected opening angle for 3-D rupture tracking of earthquakes as a function of rupture length, epicentral distances and inclination angles, while avoiding the polarization uncertainty being dropped below the noise level. Then we perform 3-D synthetic tests for rupture tracking with 6-DoF measurements.

4.1 3-D single-station opening angles

We define the opening angle of a specific station as the difference between the BAz for the starting position of the unilateral rupture and the BAz for the ending position (Bayer et al., 2012). A large opening angle is desirable to minimize uncertainties which corresponds to a short distance between receivers and earthquakes. But the distance has to be large enough to fulfill the assumption of a plane wave and it is also an important parameter because the analysis of the polarization is less efficient for signals in which many different phases are interfering.

The following description is a purely geometrical concept to demonstrate the expected scaling of opening angles. If we define the rupture path as a straight line on a sphere, we can describe the geometry between the receiver and rupture by a large triangle. In Fig. 9 we illustrate the opening angle α for fault lengths between 100 and 1000 km (blue lines) at epicentral distances d of 10°, 30°, 50° and 80° (different plotting windows). The triangle is not necessarily isosceles, which is described by the inclination angle $\delta \in [0, 90°]$. The maximum opening angle occurs for $\delta = 90°$, i.e., the station is situated perpendicular to the center of the rupture and the triangle is isosceles. In general α increases for larger faults as well as for shorter station distances. By applying the spherical law of cosines, the opening angle α can be described by the side lengths s_1, s_2 and l, where l denotes the rupture length:

$$\cos(\alpha) = \frac{\cos(l) - \cos(s_1)\cos(s_2)}{\sin(s_1)\sin(s_2)}. \tag{4}$$

The side lengths s_1 and s_2 can be expressed by δ, l and d via

$$\cos(s_{1/2}) = \cos(d)\cos(\tfrac{l}{2}) \pm \sin(d)\sin(\tfrac{l}{2})\cos(\delta). \tag{5}$$

In an epicentral distance of 30° the opening angle for a fault of 1000 km is about 18° (see upper right window). For example, the mainly unilateral Sumatra earthquake has a rupture length of about 1200 km. If we increase the inclination angle from 0° to 30° at the same distance, the opening angle decreases to about 9°. This may be still sufficient for an estimation of the spatial and temporal evolution of the rupture with a single station. Significantly shorter ruptures or very small inclination angles however, will lead to an opening angle of only a few degrees challenging tracking.

[Figure 9 about here.]

4.2 Synthetic case studies in 3-D

To verify the stability and accuracy of rupture tracking using 6-DoF measurements in 3-D, we calculate synthetic seismograms using `Instaseis`, an efficient tool for generating synthetic global seismograms using Green's function databases generated with `AxiSEM` (Driel et al., 2015) based on 1-D axisymmetric velocity models. Although `Instaseis` does not allow a direct output of rotational components, we derive them utilizing a densely spaced array, i.e., gradient based array-derived rotation. In the following synthetic tests, we place four additional stations surrounding the central station with a spatial interval of 100 m (see the upper left subplot in Fig. 10). The array-derived rotation is calculated based on a finite-difference scheme (Spudich et al., 1995; Langston, 2007), as the rotational motions will be simplified to horizontal spatial gradients of translational motions at the free surface where vertical stress equals zero (Robertsson & Curtis, 2002). `Instaseis` enables us to handle finite ruptures represented by an arbitrary number of point sources. The simulated rupture consists of six subevents and propagates approximately from south-east to north-west (indicated by the black arrow in Fig. 10). All subevents are assigned a uniform faulting mechanism (strike: 336°, rake: 114°, dip: 7°) and are evenly distributed along the fault plane at the same depth (10 km). The total rupture length is about 236 km. Considering that the rupture speed and radiated energy can be largely affected by local structural properties and stress conditions, we slightly randomize the source time functions of each subevent in terms of slip rate and initiation time (see the source time functions in Fig. 11c-d, g-h and Fig. 12c-d).

The estimated BAz at stations ST1, ST2 and ST3 with the epicentral distances of 25°, 14° and 50°respectively, is expected to continuously increase during the rupture tracking process (Fig. 10). For stations ST1 and ST2, we use the singular value decomposition (SVD) algorithm for robust ratio calculations of Eq. 2 (Vidale, 1986; Greenhalgh et al., 2018), with a sliding time window of 30 s starting from the first direct P arrival. The recorded rotational motions in the two horizontal rotational components are mostly resulting from P-converted SV-waves at the Earth surface. For station ST3, we apply the CC method to the vertical rotational component and the two horizontal translational components, in order to focus on SH-waves, with the same sliding window as the one for ST1 and ST2. We select the station ST3 with a larger epicentral distance such that the direct SH-waves can be separated in time from surface wave arrivals. We generate two datasets for each station. The BAz estimate for each dataset as a function of time is shown in Fig. 11a-b, e-f and Fig. 12a-b (dashed black lines denote the theoretical starting and ending BAz of the rupture at the given station). The corresponding source time functions are plotted in Fig. 11c-d, g-h and Fig. 12c-d.

We show that the estimated BAz during the rupture tracking process is generally accurate and consistent at all three stations (Fig. 11 and 12). However, the slope of the estimated BAz (e.g., Fig. 11a-b) is not ideally uniform. This can be mainly attributed to two factors: i) the changing onset times and slip rates across the finite source. Theoretically, the slope variation of the estimated BAz is supposed to directly indicate the changes of rupture speed as we have discussed in section 3.1. However, since we randomize the source time functions of all subevents, the slope of the estimated BAz should not be strictly invariant. ii) interferences of first and later arrivals generated by the same or different subevents. This is an issue we may have to deal with in real data analysis. In Fig. 11g, we notice that there is a weak subevent between 70 s and 90 s, which may correspond to the plateau between 260 s and 290 s in Fig. 11e. The actual BAz estimation within this period is a result of the earlier arriving stronger phases (with smaller BAzs) and later weaker phases (with bigger BAzs), which will result in a bias towards the smaller BAz when performing SVD analysis.

In contrast, with a relatively well-balanced source time function (Fig. 11h), the slope of the estimated BAz variation is equally more uniform (Fig. 11f).

[Figure 10 about here.]

[Figure 11 about here.]

[Figure 12 about here.]

5 Discussion

In this study we explore the potential of using 6-DoF observations to track large finite ruptures by 1) exploiting the correlation of translational and rotational motion observations of SH-waves and 2) exploiting the polarization filtering effect of pure horizontal rotational motions. We demonstrate for both complementary approaches that - at least theoretically - tracking ruptures is possibly provided that 6-DoF measurements are at an appropriate epicentral distance and direction from the finite source. We show that estimating the BAz as a function of time is stable enough to track earthquake rupture even in heterogeneous media. Direct estimates of rupture velocity have been derived under sub-Rayleigh and supershear variation along the fault. We also show that - as long as the rupture-induced shear waves can be identified, the directivity effect can (and should) be corrected for. The presented synthetic models are all unidirectional propagating. We do expect considerably more complexity if 1) rupture is bilateral, 2) the finite source is extremely complex and 3) complex 3-D velocity structures.

With the advent of the first broadband portable rotational seismometer systems (Bernauer et al., 2018), direct observations of 6-DoF motions of large earthquakes becomes feasible. The sensitivity of the instrument allows for recording large earthquakes with high signal-to-noise ratios. However, the source, path and site complexity reflected in real data may challenge BAz estimates. The presented methods with respect to rotational seismology are readily applicable to (combined) strain observations. With the increasing accuracy of distributed acoustic sensing (DAS) type measurements application of this method to DAS observations should be further explored (Lindsey et al., 2017; Jousset et al., 2018; Yu et al., 2019).

The severe interference of multiple types of waves may hinder the here presented application of rupture tracking methods using S-waves. However, this issue might be mitigated in case of 6-DoF measurements thanks to the inherent wavefield separation in the rotational components, i.e., only SH-waves or Loves wave are presented in vertical rotation. As is shown in Fig. 12, we are able to capture the rupture process when applying the CC method to direct SH-waves using vertical rotational component and two horizontal translational components. This provides a useful complement to classical back-projection earthquake rupture imaging which solely relies on P-wave information.

6 Conclusion

Six degree-of-freedom (6-DoF) single-station observations allow the extraction of wavefield information comparable to small-scale seismic arrays (e.g., Igel et al., 2015; Schmelzbach et al., 2018; Sollberger et al., 2018). In particular, estimates of phase velocities and subreceiver physical velocities, incidence and BAz angles are possible. We show that such 6-DoF observations allow in principle to track the location of sources of seismic energy and discuss sensitivity and challenges to methods based on cross correlation or polarization analysis, respectively. Investigating the potential of emerging 6-DoF observations in the context of earthquake physics, the developed approaches here can be generalized to arbitrary sources of seismic energy as environmental sources, volcanic sources and atmospheric sources as well as distributed acoustic sensing (DAS) type measurements.

7 Acknowledgments and Data statement

We gratefully acknowledge support from the European Research Council for funding the ERC-Advanced ROMY Project (www.romy-erc.eu). A.-A.G. acknowledges support by the European Research Council (TEAR, ERC Starting grant no. 852992), by the European Union's Horizon 2020 research and innovation program (ChEESE, grant no. 823844), by the German Research Foundation (DFG) (projects no. GA 2465/2-1, GA 2465/3-1), by KAUST-CRG (GAST, grant no. ORS-2016-CRG5-3027 and FRAGEN, grant no. ORS-2017-CRG6 3389.02), by BaCaTec (project no. A4) and BayLat and by KONWIHR – the Bavarian Competence Network for Technical and Scientific High Performance Computing (project NewWave). D.A.M. acknowledges financial support from the European Research Council under the Horizon 2020 Research and Innovation Programme grant agreement number 772255, and the Alfred P. Sloan Foundation through the Deep Carbon Observatory (DCO) Modeling and Visualization Forum.

Computing resources were provided by the Institute of Geophysics of LMU Munich (Oeser et al., 2006) and the Leibniz Supercomputing Centre (LRZ, projects no. pr63qo and pr45fi on SuperMUC).

The open-source 2-D wave propagation package `se2wave` is available at `https://bitbucket.org/dmay/se2wave`. The 3-D experiments use the openly accessible software `instaseis` `http://instaseis.net`, which databases are hosted by the IRIS DMC via the

Syngine webservice backend Krischer et al. (2017). All synthetic datasets used in this study are available on request from the corresponding author.

We specifically thank Jean-Paul Ampuero for fruitful discussions inspiring this study.

References

Aki, K., & Richards, P. G. (2002). *Quantitative seismology.* University Science Book.

Ammon, C. J., Ji, C., Thio, H.-K., Robinson, D., Ni, S., Hjorleifsdottir, V., ... others (2005). Rupture process of the 2004 sumatra-andaman earthquake. *Science*, *308*(5725), 1133–1139.

Archuleta, R. J. (1984). A faulting model for the 1979 imperial valley earthquake. *Journal of Geophysical Research: Solid Earth*, *89*(B6), 4559–4585.

Balay, S., Abhyankar, S., Adams, M. F., Brown, J., Brune, P., Buschelman, K., ... Zhang, H. (2019). *PETSc users manual* (Tech. Rep. No. ANL-95/11 - Revision 3.12). Argonne National Laboratory. Retrieved from `https://www.mcs.anl.gov/petsc`

Balay, S., Gropp, W. D., McInnes, L. C., & Smith, B. F. (1997). Efficient management of parallelism in object oriented numerical software libraries. In E. Arge, A. M. Bruaset, & H. P. Langtangen (Eds.), *Modern software tools in scientific computing* (pp. 163–202). Birkhäuser Press.

Bayer, B., Kind, R., Hoffmann, M., Yuan, X., & Meier, T. (2012). Tracking unilateral earthquake rupture by p-wave polarization analysis. *Geophysical Journal International*, *188*(3), 1141–1153.

Bernauer, F., Wassermann, J., Guattari, F., Frenois, A., Bigueur, A., Gaillot, A., ... Igel, H. (2018). Blueseis3a: Full characterization of a 3c broadband rotational seismometer. *Seismological Research Letters*.

Bernauer, F., Wassermann, J., & Igel, H. (2012). Rotational sensorsa comparison of different sensor types. *Journal of seismology*, *16*(4), 595–602.

Cochard, A., Igel, H., Schuberth, B., Suryanto, W., Velikoseltsev, A., Schreiber, U., ... Vollmer, D. (2006). Rotational motions in seismology: theory, observation, simulation. In *Earthquake source asymmetry, structural media and rotation effects* (pp. 391–411). Springer.

Driel, M. v., Krischer, L., Stähler, S. C., Hosseini, K., & Nissen-Meyer, T. (2015). Instaseis: Instant global seismograms based on a broadband waveform database. *Solid Earth*, *6*(2), 701–717.

Edme, P., & Yuan, S. (2016). Local dispersion curve estimation from seismic ambient noise using spatial gradients. *Interpretation*, *4*(3), SJ17–SJ27.

Flinn, E. (1965). Signal analysis using rectilinearity and direction of particle motion. *Proceedings of the IEEE*, *53*(12), 1874–1876.

Frohlich, C., & Pulliam, J. (1999). Single-station location of seismic events: A review and a plea for more research. *Physics of the Earth and Planetary Interiors*, *113*(1-4), 277–291.

Gabriel, A., Ampuero, J., Dalguer, L. A., & Mai, P. M. (2012). The transition of dynamic rupture styles in elastic media under velocity-weakening friction. *J. Geophys. Res.*, *117*(B9). Retrieved from https://agupubs.onlinelibrary.wiley.com/doi/abs/10.1029/2012JB009468 doi: 10.1029/2012JB009468

Graizer, V., & Kalkan, E. (2008). Response of pendulums to complex input ground motion. *Soil Dynamics and Earthquake Engineering*, *28*(8), 621–631.

Greenhalgh, S., Mason, I., & Zhou, B. (2005). An analytical treatment of single station triaxial seismic direction finding. *Journal of Geophysics and Engineering*, *2*(1), 8.

Greenhalgh, S., Sollberger, D., Schmelzbach, C., & Rutty, M. (2018). Single-station polarization analysis applied to seismic wavefields: A tutorial. *Advances in Geophysics*, *59*, 123–170.

Hadziioannou, C., Gaebler, P., Schreiber, U., Wassermann, J., & Igel, H. (2012). Examining ambient noise using colocated measurements of rotational and translational motion. *Journal of seismology*, *16*(4), 787–796.

Huang, B.-S. (2003). Ground rotational motions of the 1999 chi-chi, taiwan earthquake as inferred from dense array observations. *Geophysical Research Letters*, *30*(6).

Igel, H., Bernauer, M., Wassermann, J., & Schreiber, K. U. (2015). Rotational seismology: Theory, instrumentation, observations, applications. *Encyclopedia of Complexity and Systems Science*, 1–26.

Igel, H., Cochard, A., Wassermann, J., Flaws, A., Schreiber, U., Velikoseltsev, A., & Pham Dinh, N. (2007). Broad-band observations of earthquake-induced rotational ground motions. *Geophysical Journal International*, *168*(1), 182–196.

Ishii, M., Shearer, P. M., Houston, H., & Vidale, J. E. (2005). Extent, duration and speed of the 2004 sumatra–andaman earthquake imaged by the hi-net array. *Nature*, *435*(7044), 933.

Jousset, P., Reinsch, T., Ryberg, T., Blanck, H., Clarke, A., Aghayev, R., … Krawczyk, C. M. (2018). Dynamic strain determination using fibre-optic cables allows imaging of seismological and structural features. *Nature communications*, *9*(1), 2509.

Kiser, E., & Ishii, M. (2017). Back-projection imaging of earthquakes. *Annual Review of Earth and Planetary Sciences*, *45*(1), 271-299. doi: 10.1146/annurev-earth-063016-015801

Krischer, L., Hutko, A. R., Van Driel, M., Stähler, S., Bahavar, M., Trabant, C., & Nissen-Meyer, T. (2017). On-demand custom broadband synthetic seismograms. *Seismological Research Letters*, *88*(4), 1127–1140.

Krüger, F., & Ohrnberger, M. (2005). Tracking the rupture of the m w= 9.3 sumatra earthquake over 1,150 km at teleseismic distance. *Nature*, *435*(7044), 937.

Langston, C. A. (2007). Spatial gradient analysis for linear seismic arrays. *Bulletin of the*

Seismological Society of America, *97*(1B), 265–280.

Langston, C. A., & Liang, C. (2008). Gradiometry for polarized seismic waves. *Journal of Geophysical Research: Solid Earth*, *113*(B8).

Lindsey, N. J., Martin, E. R., Dreger, D. S., Freifeld, B., Cole, S., James, S. R., ... Ajo-Franklin, J. B. (2017). Fiber-optic network observations of earthquake wavefields. *Geophysical Research Letters*, *44*(23), 11–792.

Mai, P. M., Schorlemmer, D., Page, M., Ampuero, J.-P., Asano, K., Causse, M., ... others (2016). The earthquake-source inversion validation (SIV) project. *Seismological Research Letters*, *87*(3), 690–708. doi: 10.1785/0220150231

McGuire, J. J., & Kaneko, Y. (2018, 06). Directly estimating earthquake rupture area using second moments to reduce the uncertainty in stress drop. *Geophysical Journal International*, *214*(3), 2224-2235. Retrieved from `https://doi.org/10.1093/gji/ggy201` doi: 10.1093/gji/ggy201

Montalbetti, J. F., & Kanasewich, E. R. (1970). Enhancement of teleseismic body phases with a polarization filter. *Geophysical Journal International*, *21*(2), 119–129.

Oeser, J., Bunge, H.-P., & Mohr, M. (2006). Cluster design in the earth sciences: Tethys. In *International conference on high performance computing and communications* (pp. 31–40).

Pancha, A., Webb, T., Stedman, G., McLeod, D., & Schreiber, K. (2000). Ring laser detection of rotations from teleseismic waves. *Geophysical Research Letters*, *27*(21), 3553–3556.

Pham, N. D., Igel, H., de la Puente, J., Käser, M., & Schoenberg, M. A. (2010). Rotational motions in homogeneous anisotropic elastic media. *Geophysics*, *75*(5), D47–D56.

Robertsson, J. O., & Curtis, A. (2002). Wavefield separation using densely deployed three-component single-sensor groups in land surface-seismic recordings. *Geophysics*, *67*(5), 1624–1633.

Schmelzbach, C., Donner, S., Igel, H., Sollberger, D., Taufiqurrahman, T., Bernauer, F., ... Robertsson, J. (2018). Advances in 6-c seismology: applications of combined translational and rotational motion measurements in global and exploration seismology. *Geophysics*, *83*(3), 1–58.

Schmidt, R. (1986). Multiple emitter location and signal parameter estimation. *IEEE transactions on antennas and propagation*, *34*(3), 276–280.

Schreiber, K. U., & Wells, J.-P. R. (2013). Invited review article: Large ring lasers for rotation sensing. *Review of Scientific Instruments*, *84*(4), 041101.

Shimizu, K., Yagi, Y., Okuwaki, R., & Fukahata, Y. (2019, 11). Development of an inversion method to extract information on fault geometry from teleseismic data. *Geophysical*

Journal International. Retrieved from `https://doi.org/10.1093/gji/ggz496` (ggz496) doi: 10.1093/gji/ggz496

Sollberger, D., Greenhalgh, S. A., Schmelzbach, C., Van Renterghem, C., & Robertsson, J. O. (2018). 6-c polarization analysis using point measurements of translational and rotational ground-motion: theory and applications. *Geophysical Journal International*, *213*(1), 77–97.

Spudich, P., & Fletcher, J. B. (2009). Software for inference of dynamic ground strains and rotations and their errors from short baseline array observations of ground motions. *Bulletin of the Seismological Society of America*, *99*(2B), 1480–1482.

Spudich, P., Steck, L. K., Hellweg, M., Fletcher, J., & Baker, L. M. (1995). Transient stresses at parkfield, california, produced by the m 7.4 landers earthquake of june 28, 1992: Observations from the upsar dense seismograph array. *Journal of Geophysical Research: Solid Earth*, *100*(B1), 675–690.

Suryanto, W., Igel, H., Wassermann, J., Cochard, A., Schuberth, B., Vollmer, D., ... Velikoseltsev, A. (2006). First comparison of array-derived rotational ground motions with direct ring laser measurements. *Bulletin of the Seismological Society of America*, *96*(6), 2059–2071.

Ulrich, T., Gabriel, A.-A., Ampuero, J.-P., & Xu, W. (2019, December). Dynamic viability of the 2016 Mw 7.8 Kaikura earthquake cascade on weak crustal faults. *Nature Communications*, *10*(1), 1213. doi: 10.1038/s41467-019-09125-w

van Driel, M., Wassermann, J., Pelties, C., Schiemenz, A., & Igel, H. (2015). Tilt effects on moment tensor inversion in the near field of active volcanoes. *Geophysical Journal International*, *202*(3), 1711–1721.

Vidale, J. E. (1986). Complex polarization analysis of particle motion. *Bulletin of the Seismological society of America*, *76*(5), 1393–1405.

Yu, C., Zhan, Z., Lindsey, N. J., Ajo-Franklin, J. B., & Robertson, M. (2019). The potential of das in teleseismic studies: Insights from the goldstone experiment. *Geophysical Research Letters*, *46*(3), 1320–1328.

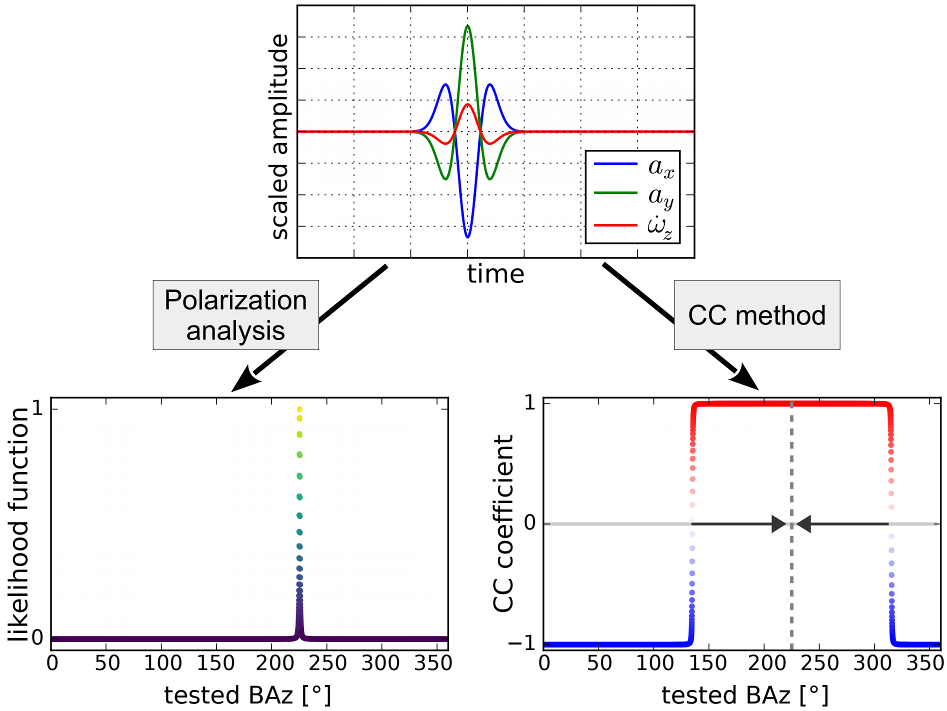

Figure 1. The actual BAz of 225° for a plane SH-wave can be estimated by the CC method and the polarization analysis. **Top**: the seismogram of an ideal SH-wave at the free surface contains three nonzero components (the horizontal accelerations a_x , a_y and the vertical rotation rate $\dot{\omega}_z$). **Bottom Left**: the grid search result of the polarization analysis. The normalized likelihood function has a maximum at 225°. **Bottom Right**: the grid search result of the CC method. The zero-lag CC coefficient as a function of the tested BAz has the shape of a step function. The BAz is correctly estimated by determining the central point between the zero-transitions (indicated by arrows).

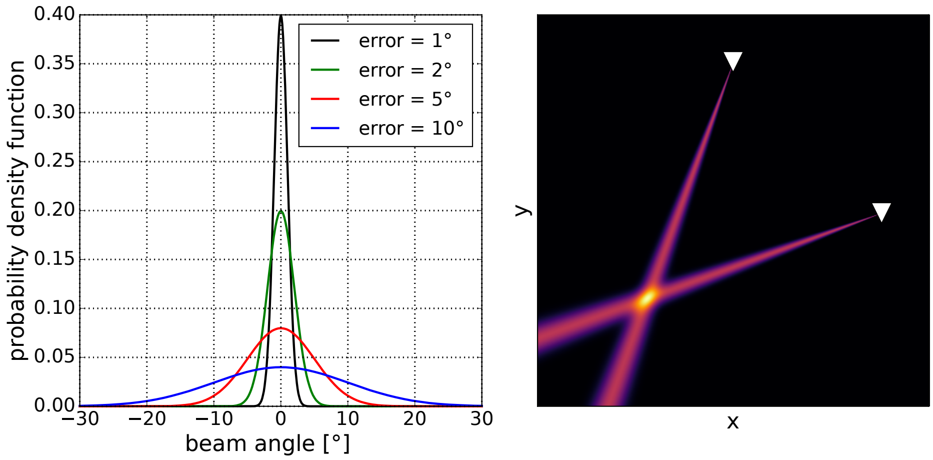

Figure 2. The BAz uncertainties can be described by probability density functions. **Left:** each curve shows the probability density function for a specific BAz error σ. The beam angle describes the broadness around the estimated BAz which corresponds to 0°. **Right:** Eq. 3 is illustrated in 2-D at a certain time-step for two stations (white triangles). An expected error of $\sigma = 1.5^\circ$ describes the broadness of each beam. The highest value (yellow area) is expected to be close to the source position.

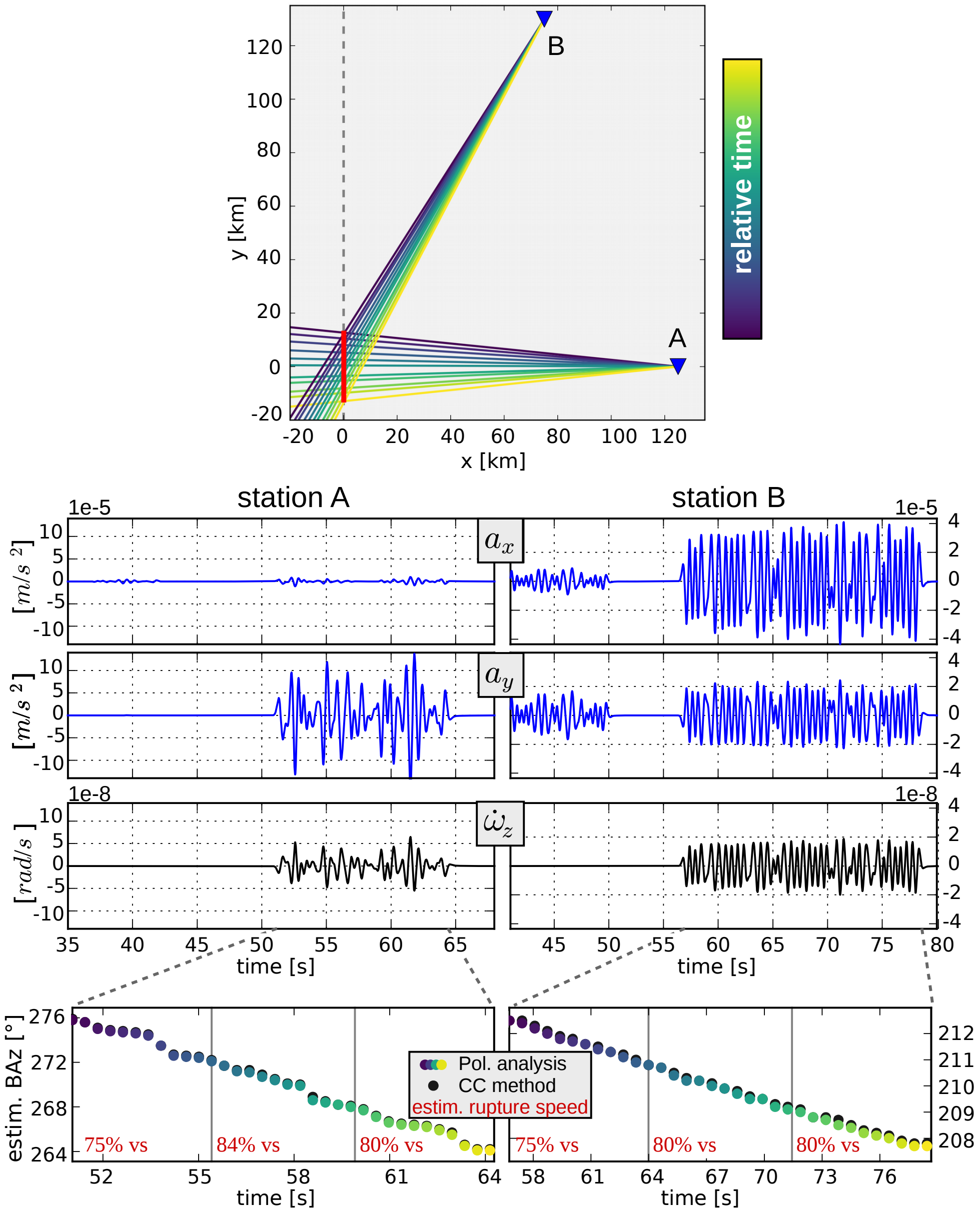

Figure 3. Using SH-waves for rupture tracking in a single station approach. **Top:** rupture (red line) and receiver positions (blue triangles) are shown in horizontal dimensions x, y. The color-coded rays indicate the estimated BAz variations at each station. The rupture is correctly tracked. **Middle:** recorded seismograms of horizontal accelerations a_x , a_y and vertical rotation rate $\dot{\omega}_z$. **Bottom:** the BAz is estimated by two different methods in the direct SH-arrivals. The estimations are divided into three sub-windows in which the rupture speed is determined. The true rupture velocity is 80% v_s.

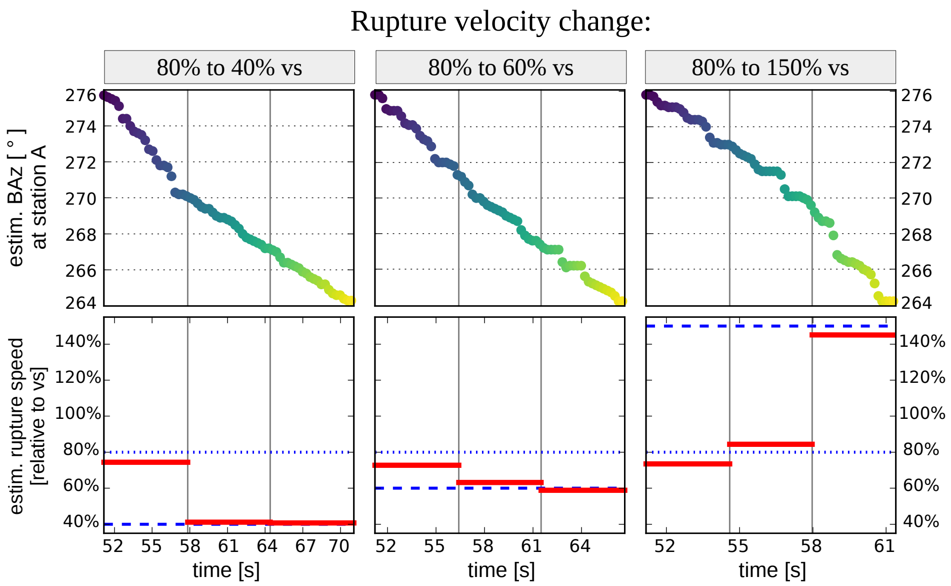

Figure 4. Tracking variations in rupture velocity at station A. The first half of the rupture breaks with 80% of the shear-wave velocity v_s, the second half breaks with 40%, 60% or 150% v_s. The BAz variation is estimated in the SH-arrivals at station A (see Fig. 3). The results are represented by a red horizontal line in each subwindow. The actual velocities are indicated by blue dashed lines. For consistency reasons, we use the same color-scale from yellow to blue in the upper subplots.

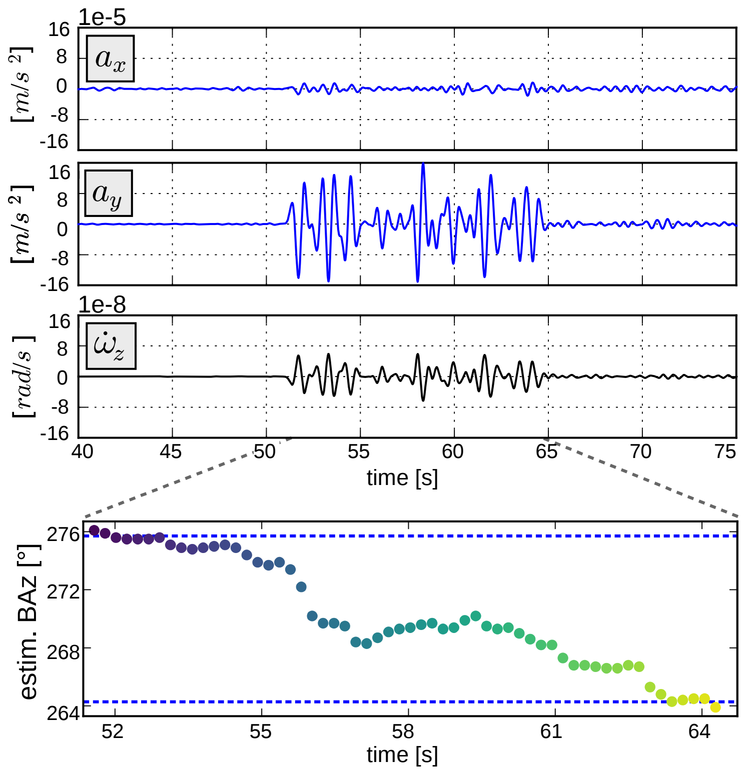

Figure 5. Rupture tracking in a heterogeneous material at station A. Density, P-wave and S-wave velocity are perturbed independently in each material cell. **Top:** seismograms of horizontal accelerations a_x , a_y and vertical rotation rate $\dot{\omega}_z$. **Bottom:** result of the BAz estimation. The true BAz for start- and end-position of the rupture is marked by blue dashed lines.

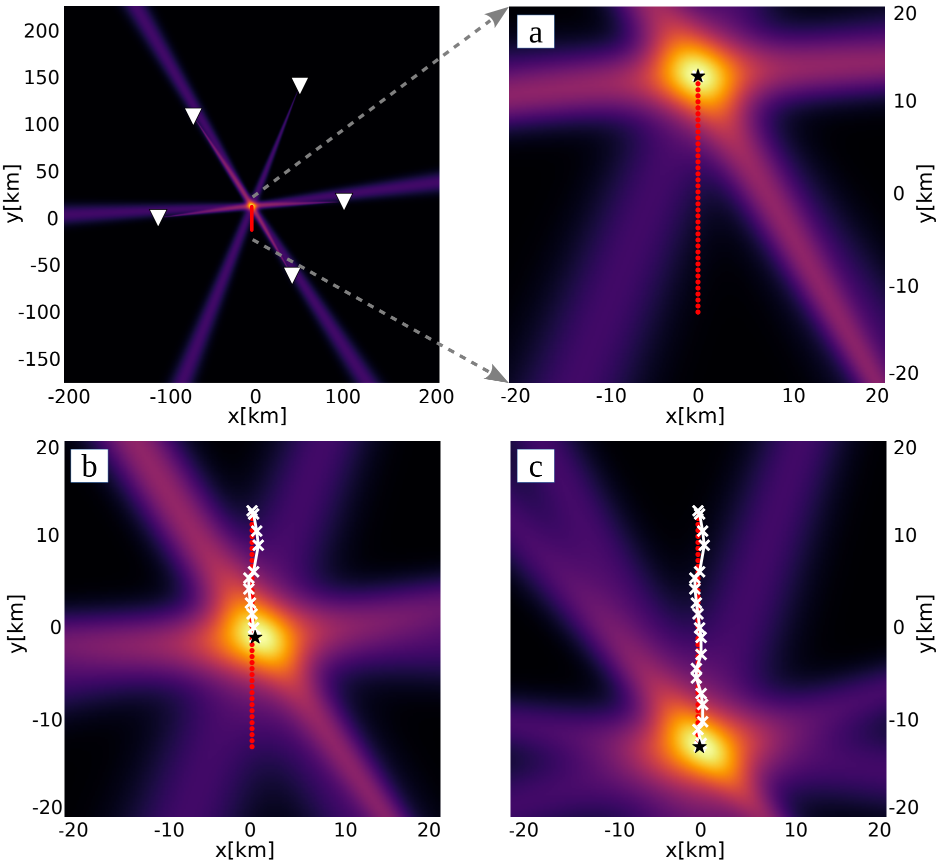

Figure 6. A unilateral rupture (red dots) is observed at five stations (white triangles) in two spatial dimensions x, y. At each station, the BAz change is estimated independently and is corrected for directivity effects. The subplots a, b and c show the result at different time-steps, where the most likely source locations are marked by a black star and white crosses indicating current and past time steps, respectively. An animation of the continuous rupture imaging process is provided in the supporting material (Movie S1: ms01.mov).

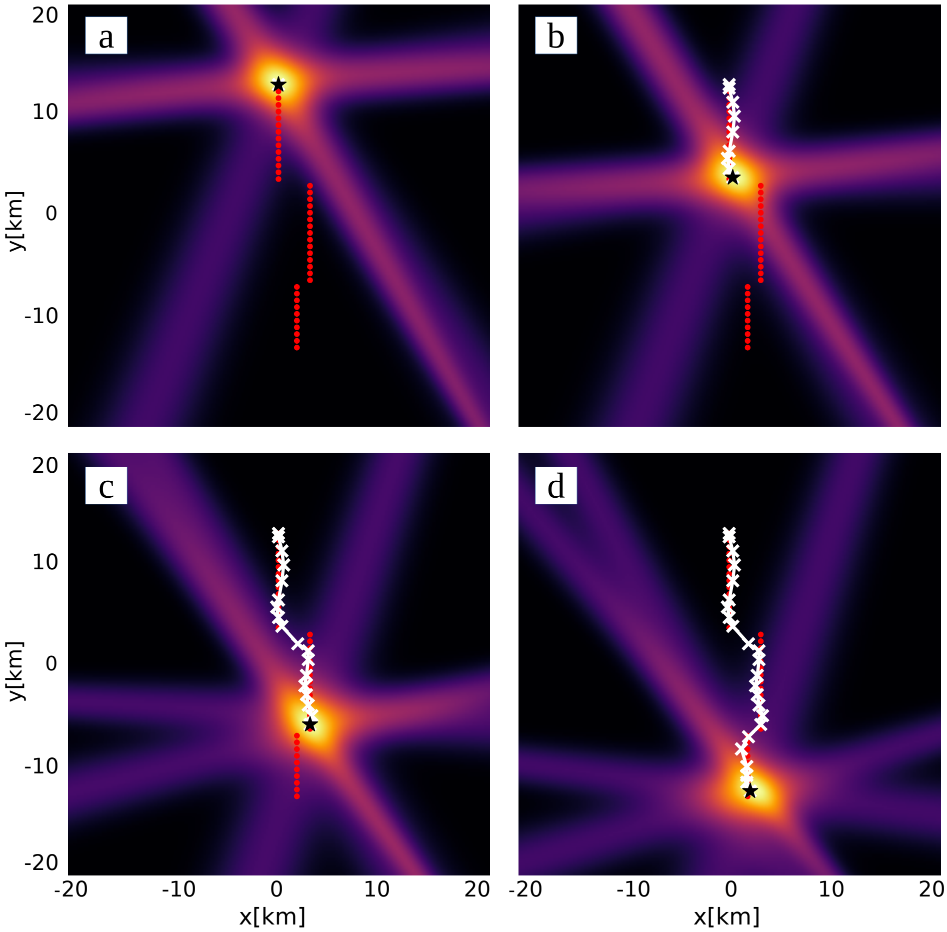

Figure 7. Rupture tracking for a more complex fault geometry. Station locations and model parameters are the same as in Fig. 6. The rupture has two spatial offsets. The windows a, b, c and d show the tracking at different time steps. An animation of the continuous rupture imaging process is provided in the supporting material (Movie S2: ms02.mov).

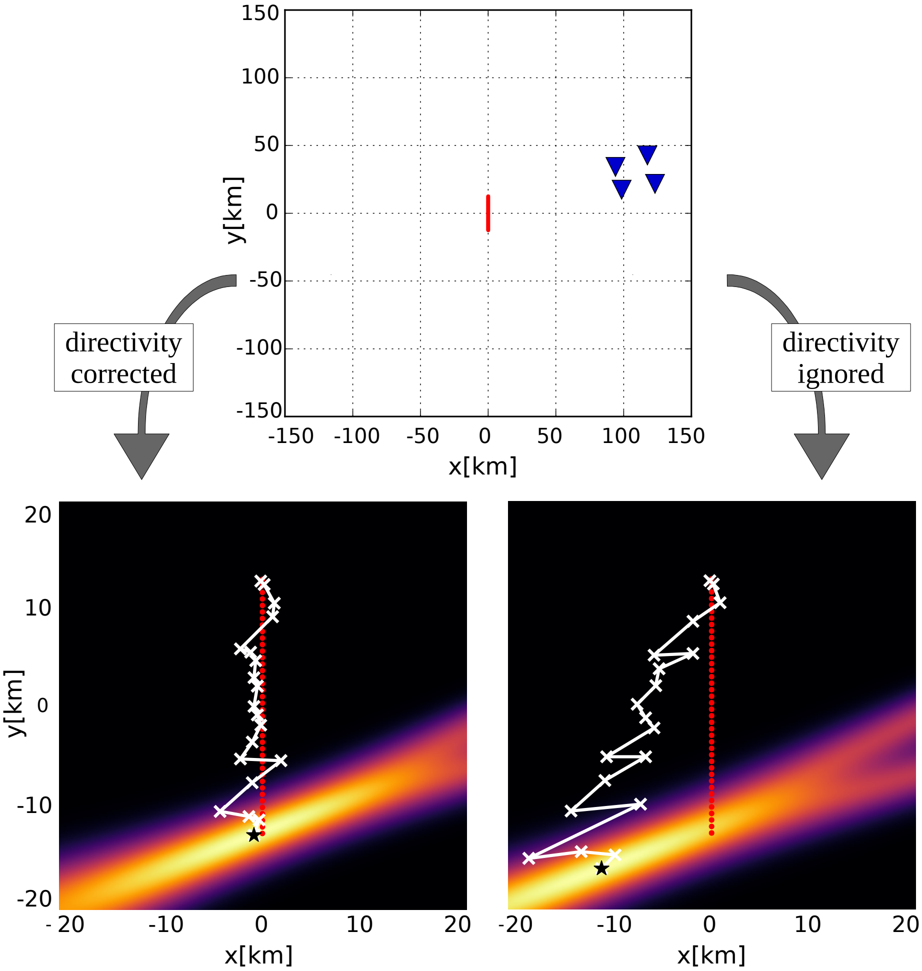

Figure 8. Influences of directivity effects on the combination of tracking results. A rupture is tracked with four stations in a small network (blue triangles). The rupture properties are the same as in Fig. 6. The bottom left shows the tracking result for corrected directivity effects. The bottom right figure shows the results for neglecting directivity effects.

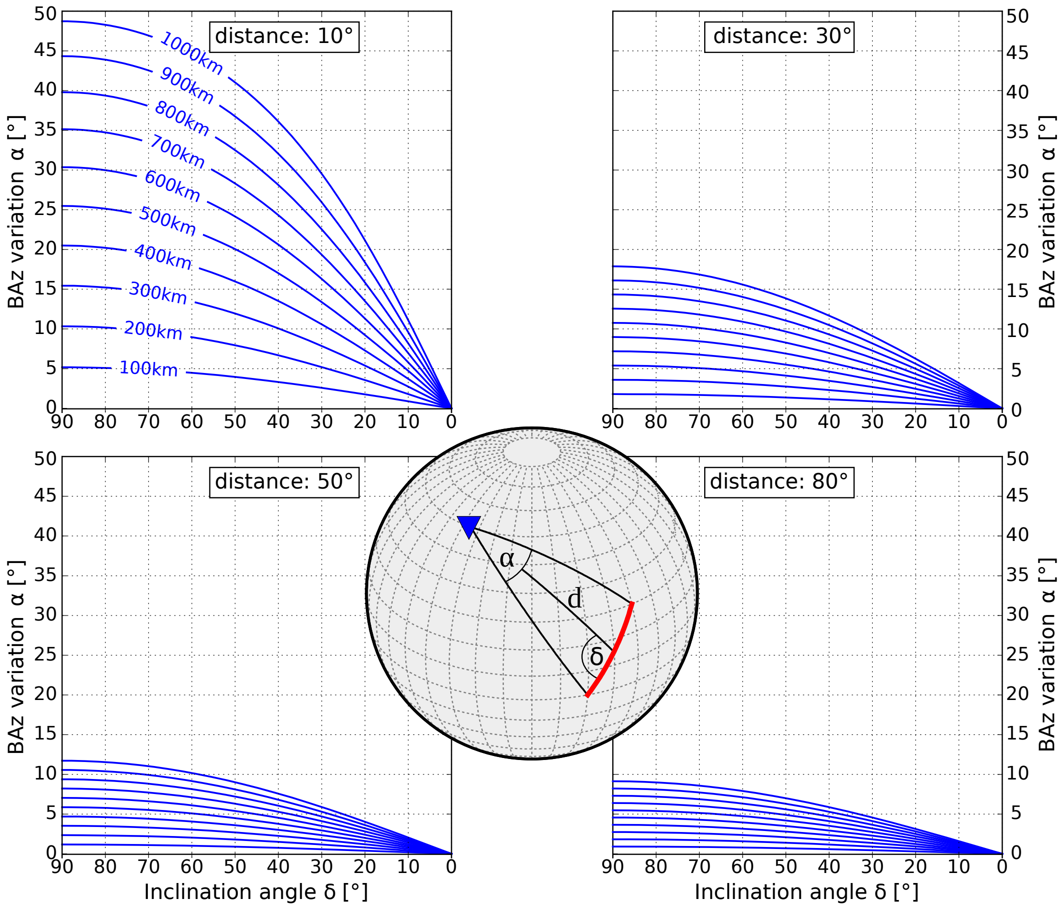

Figure 9. The opening angle α for a single station depends on the epicentral distance d, the inclination angle δ and the rupture length. The rupture path is illustrated as a red line on a sphere. The opening angle is calculated for four different distances and in each subplot for fault lengths between 100 and 1000 km. (adapted from (Bayer et al., 2012)).

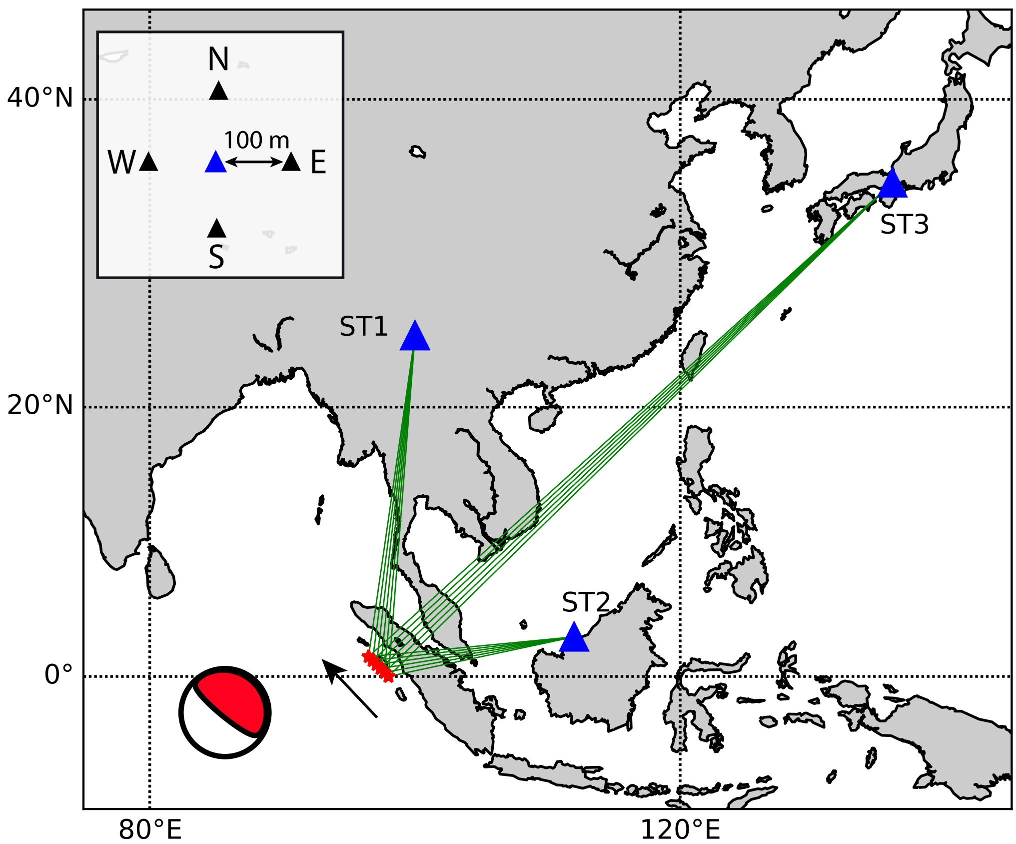

Figure 10. Modeled unilateral earthquake rupture and three teleseismic seismic stations ST1, ST2 and ST3 (blue triangles). Red dots denote the subevents of the rupture process. The beach ball in the left-bottom corner denotes the uniform focal mechanism of all subevents. The black arrow indicates the rupture direction. The upper left subplot illustrates the surrounding four stations which are used to derive rotational motions at the central station.

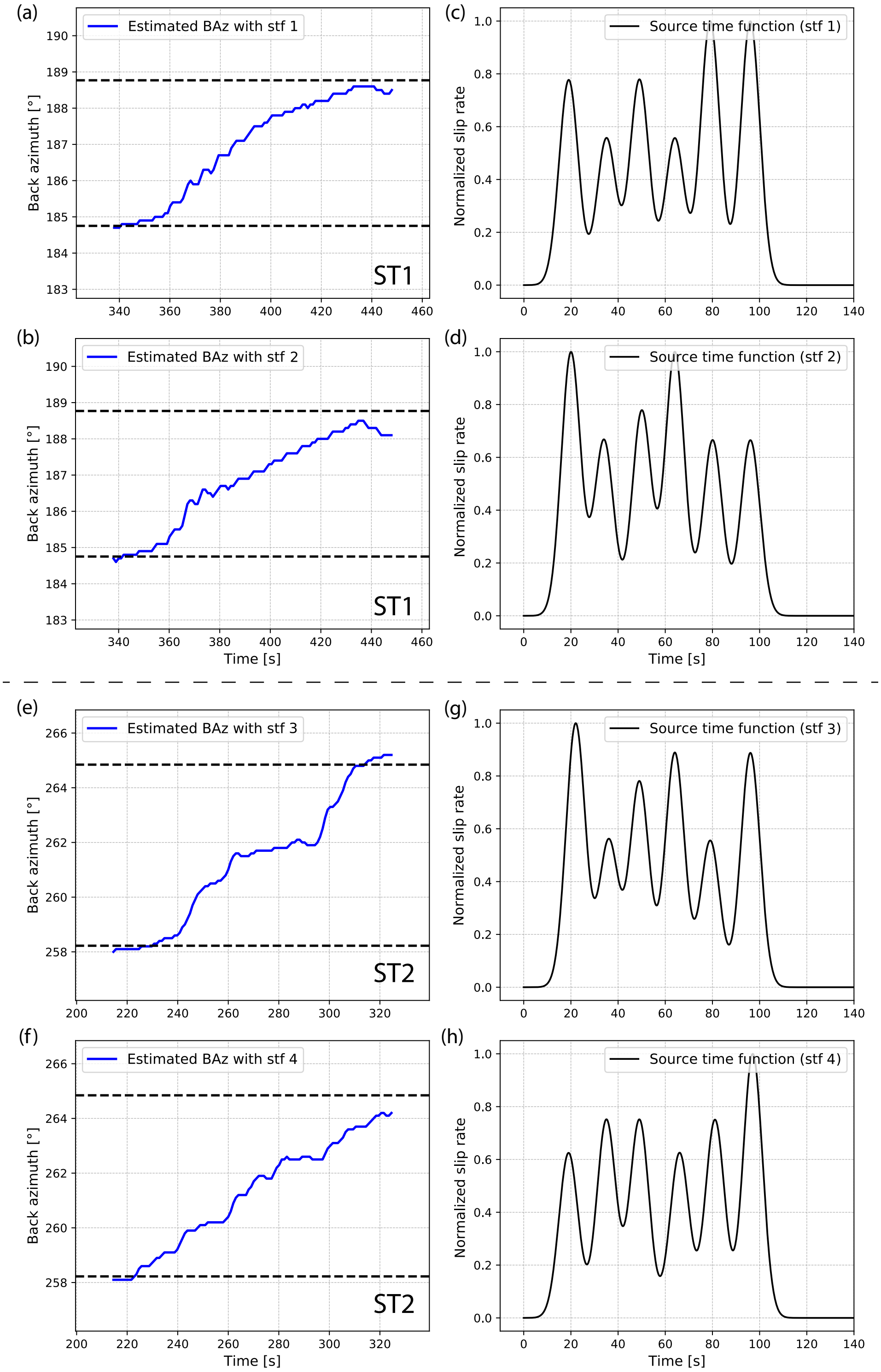

Figure 11. Upper panel (a-d): the tracked BAz variation as a function of time for two synthetic datasets in 3-D heterogeneous media at station ST1 and the corresponding source time functions (stf 1-4). The blue lines simply connect all estimated BAz of each sliding window and the dashed black lines denote the theoretical starting and ending BAz of the rupture. Bottom panel (e-h): the same as the upper panels but at the station ST2.

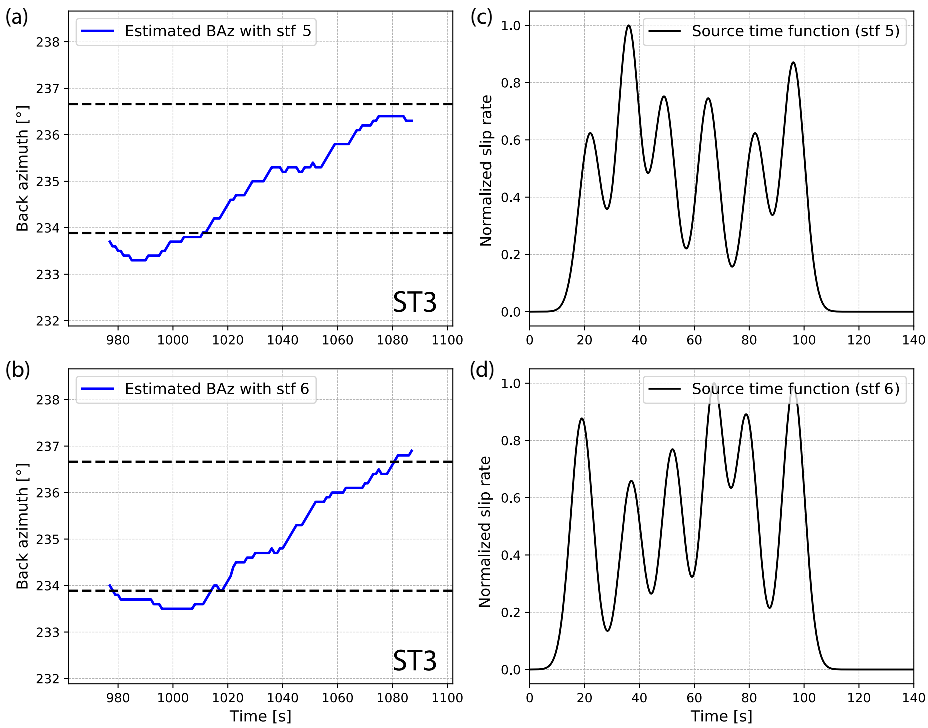

Figure 12. The same as Fig. 11 but using direct SH-waves recorded at station ST3.